

# A study of mixing in thermocapillary flows on micropatterned surfaces

BY A. A. DARHUBER<sup>1,2</sup>, J. Z. CHEN<sup>2</sup>, J. M. DAVIS<sup>1</sup> AND S. M. TROIAN<sup>1</sup>

<sup>1</sup>*Microfluidic Research and Engineering Laboratory,  
Department of Chemical Engineering, and*

<sup>2</sup>*Department of Electrical Engineering, Princeton University,  
Princeton, NJ 08544, USA (darhuber@princeton.edu)*

*Published online 12 March 2004*

The recent introduction of actuation mechanisms for microfluidic transport based on free surface flows raises a number of interesting questions involving efficient mixing configurations, especially in systems with small aspect ratios. This work investigates the characteristics of convective and diffusive mixing in continuous-mode streaming of thermocapillary microflows on chemically micropatterned surfaces. Mixing times and mixing lengths relevant to chemical microreactors or gas sensors are investigated for various geometries and parameter ranges. Scaling arguments and full numerical solutions are presented to extract optimal operating conditions. Confocal fluorescence microscopy measurements of the interfacial diffusive broadening in adjacent flowing streams confirm numerical predictions. Three important mixing regimes, based on analogues of purely diffusive dynamics, Rhines–Young shear-augmented diffusion and Taylor–Aris dispersion are identified and investigated for use in free surface flows with large surface-to-volume ratios.

**Keywords:** thermocapillary flow; mixing; microfluidics

## 1. Introduction

Rapid mixing of separate liquid volumes can pose a significant challenge, depending on the geometry and size of the container as well as the flow characteristics. For large liquid volumes, turbulent flow imparted by stirrers can greatly decrease the mixing time. For ultrasmall volumes in the sub-picolitre range, molecular diffusion suffices. Intermediate volumes ranging from nanolitres to millilitres typically necessitate skillful combinations of convective and diffusive mixing in order to reduce the mixing time to acceptable levels (Miyake *et al.* 1993; Schwesinger *et al.* 1996; Knight *et al.* 1998; Hitt & Lowe 1999; Deshmukh & Liepmann 2000; Liu *et al.* 2000; Ismagilov *et al.* 2000; Kamholz & Yager 2001; Handique & Burns 2001; Stroock *et al.* 2002). For mesoscale dimensions, the majority of schemes rely on either convective flow patterns designed to increase substantially the interfacial area between liquid samples or narrow flow constrictions where the diffusive time-scale decreases quadratically with the effective system size. Efficient design can attain rapid mixing

One contribution of 11 to a Theme ‘Transport and mixing at the microscale’.

times or short mixing distances independent of the liquid material properties or the device operating parameters.

Microfluidic devices require a combination of convection and diffusion because of the small Reynolds numbers inherent in microscale flows. Mixing lengths must also be minimized to allow for as compact a platform as possible. Many previous studies of mixing at the microscale have focused exclusively on internal flows in cylindrical or rectangular conduits. There now exist, however, several actuation techniques based on free surface flows whereby liquid streams or droplets can be propelled along the surface of a solid substrate. This work examines mixing phenomena in continuous mode streaming of thin and narrow liquid rivulets. Thermocapillary stresses are used to flow microstreams along the open surface of a substrate which is chemically patterned to confine flow along completely wettable microstripes (Darhuber *et al.* 2003*a*). In practice this is achieved by embedding electronically addressable microheaters within a glass or silicon substrate whose surface is patterned into silanized (non-wetting) and unsilanized wettable regions. For the studies reported here, a constant temperature gradient is imposed to produce a constant shear stress which drives liquid flow from warm to cool regions. Other thermal maps have been used to transport, split or coalesce discrete droplets (Darhuber *et al.* 2003*b*). Besides its use as a chemical microreactor, the open architecture design allows operation of the device as a microfluidic sensor for gases, aerosols and airborne particulates, since the microscale dimensions provide high surface-to-volume ratios for efficient capture.

This method of fluidic actuation, which relies on the presence of a free surface, introduces a number of interesting questions with regard to mixing patterns and designs for optimal mixing efficiency. For example, the chemical patterning and the small dimensions generate liquid rivulets with a cross-sectional shape that is an arc of a circle. The tapering in film thickness near the edges of the microstripe affects mixing times depending on the geometric aspect ratio. The shear driven flow is also spatially non-uniform in both the vertical and transverse directions, since the flow speed depends on the local interface height. Regions of strong interfacial curvature caused by various patterning geometries substantially affect the interface shape and consequently the mixing efficiency. Finally, the thermocapillary merging of spatially separate liquid volumes can also be strongly modified by Marangoni stresses when the surface tensions of the two liquids to be mixed are not equal (Davis *et al.* 2003).

In this article, we investigate mixing times and mixing lengths in systems consisting of liquid microstreams actuated by application of a constant thermal gradient in the streamwise direction ( $\hat{x}$ ), the transverse direction ( $\hat{y}$ ) or both. Numerical studies of the convective–diffusive equation coupled with the liquid shape along straight wettable stripes or at Y-type junctions reveal several mixing regimes and indicate favourable convection patterns for maximizing the area available for diffusive transport. Optimal operating conditions for efficient mixing with constant temperature gradients are identified. Measurements of the interface broadening of two merging streams using confocal fluorescence microscopy (CFM) show excellent agreement with numerical predictions.

## 2. Theoretical model and parameter ranges

Several investigators have previously examined the base states and stability criteria for thermocapillary flow of a thin film on a chemically *homogeneous* substrate

(Kataoka & Troian 1997; Golovin *et al.* 2001; Davis *et al.* 2003; Grigoriev 2003). The dynamics of a single-component liquid advancing on a completely wetting microstripe lithographically defined on a non-wetting surface has also been explored (Darhuber *et al.* 2001, 2003a). The coupling of the interfacial shape and the velocity field with mass transfer and solute concentration gradients forms the basis of this work. For simplicity, all liquids are assumed to be non-volatile. Except for the mixing studies involving Y-junctions, only the thermal dependence of the surface tension (which decreases linearly with increasing temperature  $T$ ) is retained—the viscosity and molecular diffusion coefficients are assumed constant. For the parameter range of interest, the thermal Péclet number based on the film height and the Biot number are very small, such that variations in temperature across the film thickness can be ignored. The local temperature of the air–liquid interface is therefore equal to the local temperature of the solid (Darhuber *et al.* 2003a). The molecular diffusion coefficient of the tracer dye is assumed to be independent of the concentration  $c$ . Moreover, in accord with the dilute approximation, the dye tracer is simply advected with the speed of the local flow (Deen 1998). The Soret effect, which can establish persistent concentration gradients in the presence of temperature non-uniformities, is also neglected.

The equation governing the shape of the flowing liquid film is derived within the lubrication approximation such that  $\epsilon^2 = (h_{\max}/w)^2 \ll 1$  and  $\epsilon Re \ll 1$ , where  $h_{\max}$  is the maximum film thickness,  $w$  the characteristic scale in the lateral direction (i.e. the microstripe width) and  $Re$  the Reynolds number based on  $h_{\max}$  (Darhuber *et al.* 2003a). The Bond number,  $Bo = \rho gh_{\max}^2/\gamma$ , is also vanishingly small ( $g$  is the acceleration due to gravity, and  $\rho$  and  $\gamma$  are the liquid’s density and surface tension, respectively).

All numerical solutions were obtained by finite-element calculations (FEMLAB 2.2) of the convection–diffusion equation

$$\frac{\partial c}{\partial t} + \mathbf{u} \cdot \nabla c = D \left( \frac{\partial^2 c}{\partial x^2} + \frac{\partial^2 c}{\partial y^2} + \frac{\partial^2 c}{\partial z^2} \right), \quad (2.1)$$

using triangular elements with linear or quadratic basis functions. In general, the velocity field,  $\mathbf{u}$ , consists of contributions from the thermocapillary stress  $\boldsymbol{\tau} \equiv \partial\gamma/\partial T \cdot \nabla T$  and capillary pressure  $p = -\gamma \nabla^2 h(x, y)$  according to

$$\mathbf{u} = \frac{1}{\mu} \left[ \boldsymbol{\tau} z + \left( \frac{z^2}{2} - zh(x, y, t) \right) \nabla p \right]. \quad (2.2)$$

In the limit  $(h_{\max}/L)^2 \ll 1$ , *capillary* flow due to the spatial variation in surface tension can be neglected, i.e.  $\nabla p = -\nabla(\gamma \nabla^2 h) \approx -\gamma \nabla \nabla^2 h$  (Kataoka & Troian 1997). Here,  $L$  denotes a characteristic streamwise length-scale. In the numerical simulations, the parameter  $\partial\gamma/\partial T$  is assumed to be  $-1 \times 10^{-4} \text{ N m}^{-1}$  unless stated otherwise.

Figure 1a specifies the coordinate system used throughout: the  $\hat{x}$ -axis coincides with the centreline position of the microstripe ( $y = 0$ ), while the  $\hat{z}$ -axis coincides with the direction normal to the solid substrate. The terms ‘streamwise’ or ‘transverse’ denote flow along the  $\hat{x}$  or  $\hat{y}$ -axes, respectively. The diagram in figure 1b shows an example of the patterned substrates used in the mixing studies, along with characteristic dimensions. The left pattern depicts a pair of square-shaped (wetable)

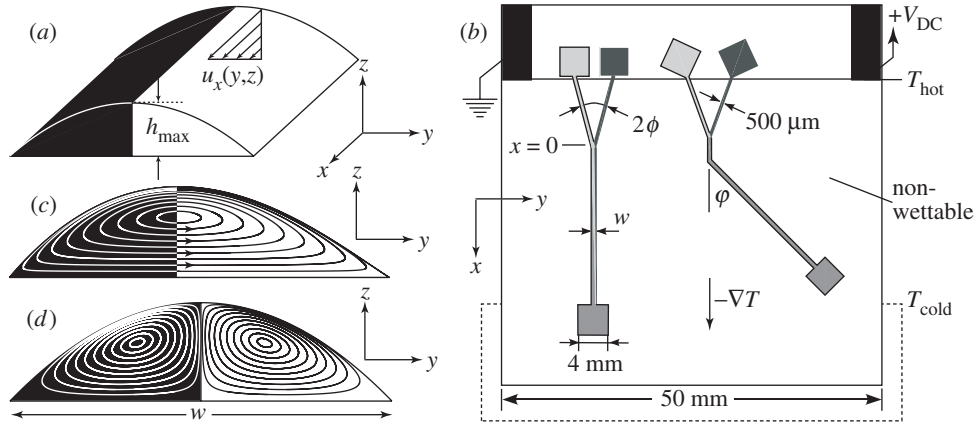


Figure 1. (a) Passive mixing geometry for two adjacent microstreams (designated by black and white regions, respectively). The velocity profile is parallel to the long axis of the rivulet and perpendicular to the concentration gradient. (b) Schematic showing two fluidic designs. White regions denote non-wettable surfaces, grey regions denote wettable surfaces. Black rectangles represent the electrical contact pads for a metallic heating resistor (horizontal black line) embedded beneath the substrate surface. The dashed rectangular area denotes a water-cooled brass block used to maintain the lower portion of the substrate at a constant temperature  $T_{\text{cold}}$ . Pure and dyed PDMS is deposited on the 4 mm wide reservoir squares, propelled along two microstrips and merges at the Y-junction. Interdiffusive broadening occurs within the merged stream of width  $w$ . Simultaneous streamwise and transverse flow is induced by orienting the merged stream at an angle  $\phi$  to the direction of  $\nabla T$ . (c), (d) Configurations for active mixing. Application of a linear or parabolic temperature profile induces either (c) single or (d) double vortical flows.

liquid reservoirs from which two distinct liquid streams flow and merge into a single (wettable) microstrip oriented parallel to  $\nabla T$ . A constant temperature gradient is generated by cooling the lower portion of the silicon substrate with a water-cooled brass block and heating the other end with a metallic thin-film resistor (horizontal black line) embedded beneath the sample surface. The pathway shown on the right of figure 1b forces the merging liquids along a microstrip that is inclined relative to  $\nabla T$  by an angle  $\phi$ . The liquids are therefore subject to thermocapillary stresses in two directions, namely  $\tau_{zx} = (\partial\gamma/\partial T) \cdot |\nabla T| \cos \phi$  and  $\tau_{zy} = (\partial\gamma/\partial T) \cdot |\nabla T| \sin \phi$ .

The substrate surface and the air–liquid interface are assumed to be non-adsorptive and impenetrable, i.e.  $\mathbf{n} \cdot \nabla c = 0$ , where  $\mathbf{n}$  represents the unit normal vector pointing outwards. In most of the problems examined, the configuration of adjacent liquid streams is assumed to be  $c(x=0, y < 0, z) = 0$  and  $c(x=0, y > 0, z) = c_0$  with  $c(x \rightarrow \infty, y) = c_0/2$ . Except for in § 3c, variables are non-dimensionalized as follows:  $\tilde{y} = 2y/w$ ,  $\tilde{z} = z/h_{\max}$ ,  $\tilde{c} = c/c_0$ ,  $\tilde{\mathbf{u}} = \mathbf{u}/u_{\max}$  and either  $\tilde{t} = t/t_{\text{mix}}$  for time-dependent or  $\tilde{x} = x/l_{\text{mix}}$  for steady-state problems. Here,  $w$  is the rivulet width,  $h_{\max}$  the rivulet apex height and  $u_{\max} = \max|\mathbf{u}|$  is the maximum flow speed. The mixing time  $t_{\text{mix}}$  and mixing length  $l_{\text{mix}}$  are determined from the criterion

$$K \equiv \frac{2}{A} \iint |\tilde{c} - \tilde{c}_{\text{av}}| dy dz < 0.05. \quad (2.3)$$

The constant  $A = 2h_{\max}w/3$  is the cross-sectional area corresponding to a rivulet

with surface shape  $h(y) = h_{\max}(1 - 4y^2/w^2)$ . The average concentration is

$$\tilde{c}_{\text{av}} = \frac{1}{A} \iint \tilde{c}(x, y, z) \, dy \, dz.$$

The factor ‘2’ is introduced to normalize  $K(t = 0)$  or  $K(x = 0)$  to unity.

Section 3 considers the case of ‘passive’ mixing wherein a transverse concentration gradient is equilibrated in the absence and presence of a streamwise thermocapillary flow. This analysis is extended to the case of flow in a Y-junction where two distinct microstreams merge onto a single microstripe. The numerical results of this study are directly compared with CFM measurements using the flow pathway shown to the left in figure 1*b*. Sections 4–6 then consider examples of ‘active’ mixing, whereby a significant decrease in mixing times can be achieved by enforcing thermocapillary flow in the transverse direction. In § 4, a thermal gradient is applied along the  $\hat{y}$ -axis as shown in figure 1*c*. In § 5, a non-uniform thermal gradient is established at the substrate surface which produces two convective rolls circulating in opposite directions as shown in figure 1*d*. Section 6 incorporates the combined action of streamwise and transverse gradients to generate helical streamlines, which considerably reduces the effective mixing length in microfluidic devices.

### 3. Passive mixing in thermocapillary flows

#### (a) Stagnant streamlets

In order to determine the relevant time-scales for diffusive mixing in the devices outlined above, it is useful to consider first the simple case of transverse diffusion in a stagnant streamlet ( $\mathbf{u} = \mathbf{0}$ ) with surface profile  $h(y) = h_{\max}(1 - 4y^2/w^2)$ . For small aspect ratios  $h_{\max}/w$ , as in the devices described, the mixing time  $t_{\text{mix}}$  is expected to scale as  $w^2/D$  and be essentially independent of  $h_{\max}$ . The numerical results in figure 2*a, b* confirm the scaling behaviour and illustrate the typical mixing times for  $h_{\max} = 40 \mu\text{m}$  and microstripe widths ranging from 100 to 900  $\mu\text{m}$ . The shape of the liquid interface, however, does modify the magnitude of the mixing time. The circles and squares represent simulations for a concave and convex liquid interface, respectively. The convex film shape reduces  $t_{\text{mix}}$  by more than 50% in comparison with the concave geometry. The solid line represents  $t_{\text{mix}}$  for a flat interface. The concave and flat interface shapes correspond to rivulets in long rectangular grooves: these conformations cannot be achieved by chemical confinement on a flat surface.

#### (b) Passive mixing with streamwise gradient

There are applications for which mixing must occur during concurrent flow and this is the case examined next. Two adjacent streams are confined to a single wettable microstripe subject to a constant thermal gradient which generates a thermocapillary flow along the  $x$ -axis. Provided that the rivulet shape  $h(y) = h_{\max}(1 - 4y^2/w^2)$  is translationally invariant along  $\hat{x}$  (i.e.  $h_{\max}$  is constant, and that the viscosity and diffusion coefficient do not depend on  $x$  to first order), the velocity field  $\mathbf{u}$  is unidirectional and fully developed, corresponding to a Couette-like profile  $u_x[0 \leq z \leq h(y)] = \tau z/\mu = u_{\max} \tilde{z}$ . For typical thermal gradients between 0.1 and 1  $\text{K mm}^{-1}$ , streaming velocities  $u_{\max}$  between 10 and 100  $\mu\text{m s}^{-1}$  and diffusion constants in the range  $(1\text{--}10) \times 10^{-11} \text{ m}^2 \text{ s}^{-1}$ , the mixing length,  $l_{\text{mix}}$ , is of the order

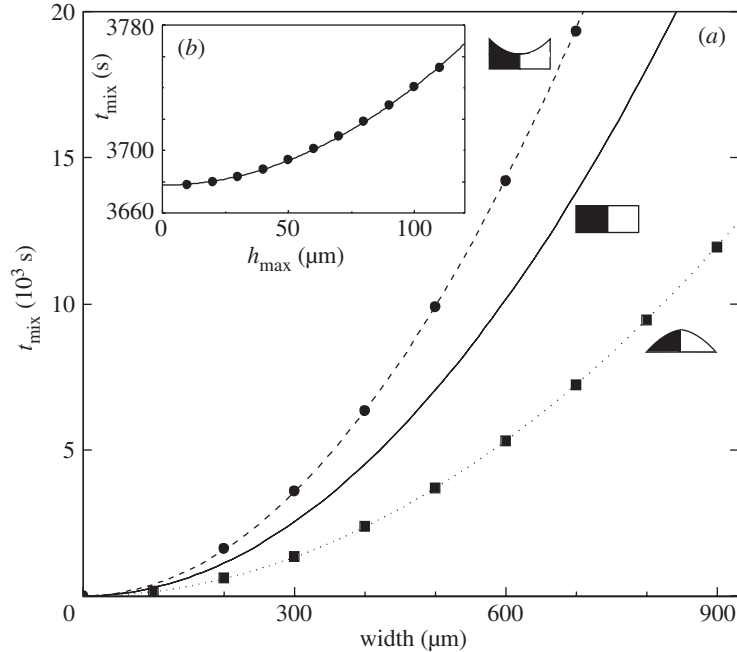


Figure 2. (a) Computed mixing times  $t_{\text{mix}}$  corresponding to purely diffusive transfer as a function of microstripe width  $w$  for  $h_{\text{max}} = 40 \mu\text{m}$  and  $D = 1 \times 10^{-11} \text{ m}^2 \text{ s}^{-1}$ . The circles and squares, which are well described by power laws  $t_{\text{mix}} \sim w^2$  (dashed, solid and dotted lines), correspond to a concave and convex rivulet surface of equal width  $w$  and centre height  $h_{\text{max}}$ , respectively. The liquid height at the edges of the concave shapes equals  $2h_{\text{max}}$ . The solid line corresponds to a flat interface. (b) Computed mixing time  $t_{\text{mix}}(h_{\text{max}})$  for a convex rivulet with  $w = 500 \mu\text{m}$ .

of 1 cm. Consequently, the Péclet number  $Pe_l = u_{\text{max}} l_{\text{mix}} / D \gg 1$ ; mass transfer by streamwise diffusion is therefore negligible in comparison with streamwise convection. Under these assumptions and steady-state conditions, equation (2.1) reduces to

$$\left(\frac{\tau}{\mu} z\right) \frac{\partial c}{\partial x} = D \left( \frac{\partial^2 c}{\partial y^2} + \frac{\partial^2 c}{\partial z^2} \right). \quad (3.1)$$

Numerical solutions quantifying the degree of diffusive intermixing were obtained from equation (3.1) by computing, as an example, the transverse position  $\delta_{0.3}(x, z)$  of the iso-concentration contour line corresponding to  $c = 0.3c_0$  for  $w = 570 \mu\text{m}$ ,  $h_{\text{max}} = 40 \mu\text{m}$  and  $D = 10^{-11} \text{ m}^2 \text{ s}^{-1}$ . As shown in figure 2c, the curve  $\delta_{0.3}(z = 0)$  naturally terminates at the microstripe edge position where  $\delta_{0.3} = w/2$ . As expected, the degree of diffusive intermixing increases with proximity to the solid surface ( $z = 0$ ) since the velocity field decreases linearly with  $z$ . Interestingly, the scaling with downstream position  $x$  also differs depending on whether  $z = 0$  or  $z > 0$ ; for example,  $\delta_{0.3}(z = 0)$  scales as  $x^{1/3}$ , whereas  $\delta_{0.3}(z > 0)$  scales for the most part as  $x^{1/2}$ .

The reason for the difference in exponents can be gleaned from equation (3.1). For small  $x$  and  $z > 0$ , the concentration profile is effectively that specified at the origin, namely  $c(x = 0, y < 0, z) = 0$  and  $c(x = 0, y > 0, z) = c_0$ . Vertical concentration gradients are therefore negligible for small  $x$ . They are also negligible sufficiently far downstream, since the small aspect ratio  $(h_{\text{max}}/w)^2 \ll 1$  ensures rapid

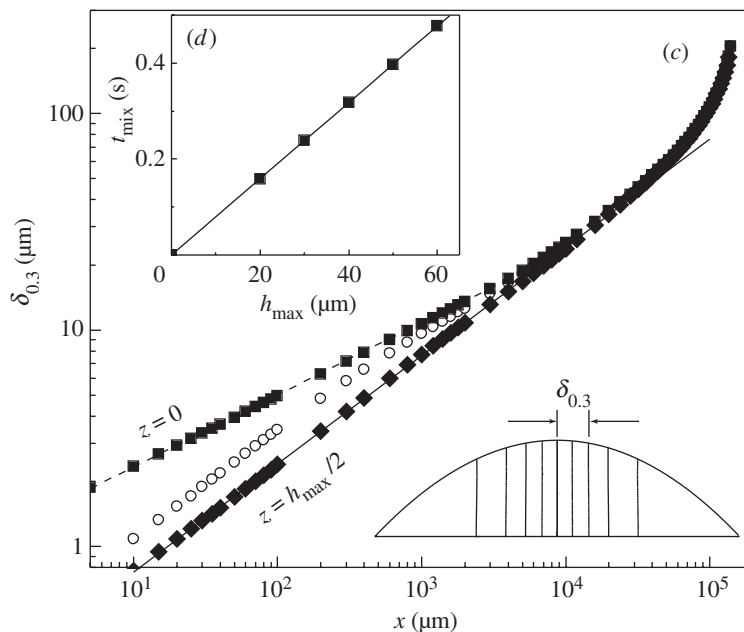


Figure 2. (Cont.) (c) Interfacial diffusive broadening,  $\delta_{0.3}(x)$ , between two adjacent liquid streams (dyed and undyed,  $w = 570 \mu\text{m}$ ,  $h_{\text{max}} = 40 \mu\text{m}$ ,  $D = 1 \times 10^{-11} \text{m}^2 \text{s}^{-1}$ ) as tracked by the dye iso-concentration line corresponding to  $\tilde{c}(x, z) = 0.3$  at three distances from the substrate surface  $z = 0$ ,  $h_{\text{max}}/4$  and  $h_{\text{max}}/2$ . At the bottom surface  $\delta_{0.3}(x, z = 0)$  scales as  $x^{1/3}$  (dashed line). Away from the substrate surface, e.g. at  $z = h_{\text{max}}/2$ ,  $\delta_{0.3}(x, h_{\text{max}}/2)$  scales as  $x^{1/2}$  (solid line). The lower right diagram shows an example of the distribution of iso-concentration lines for  $\tilde{c} = 0.1, 0.2, \dots, 0.9$  along with the definition of  $\delta_{0.3}(x, z)$ . (d) Mixing length  $l_{\text{mix}}$  as a function of  $h_{\text{max}}$  for  $w = 570 \mu\text{m}$  and  $D = 1.0 \times 10^{-11} \text{m}^2 \text{s}^{-1}$ .

equilibration of vertical gradients. A scaling analysis which balances the longitudinal convection term with the transverse diffusion term therefore determines that the width of the intermixed region increases with  $x$  according to  $\delta \sim (\mu D x / \tau z)^{1/2}$ . This scaling prediction, which as a consequence of the linear velocity profile diverges as  $z^{-1/2}$ , fails to hold at  $z = 0$ . It also fails to hold in downstream regions where the coupling of the shear flow to the concentration field generates non-negligible vertical concentration gradients. For the latter case, a scaling analysis which treats all three terms in equation (2.1) as comparable instead yields the behaviour  $\delta \sim (\mu D x / \tau)^{1/3}$ . The  $\frac{1}{3}$  exponent is evident in the intermediate downstream region of the curve  $\delta_{0.3}(z = h_{\text{max}}/4)$  in figure 2c.

The behaviour of the intermixed region at  $z = 0$  is singular, since the velocity field vanishes at the substrate surface. In this case, differentiation of equation (3.1) with respect to  $z$  yields

$$\frac{\tau}{\mu} \frac{\partial c}{\partial x} + \frac{\tau}{\mu} z \frac{\partial^2 c}{\partial x \partial z} = D \frac{\partial^3 c}{\partial y^2 \partial z} + D \frac{\partial^3 c}{\partial z^3}. \quad (3.2)$$

Evaluation of this equation at the boundary  $z = 0$ , where the impenetrability condition requires  $\partial c / \partial z(z = 0) = 0$ , causes the mixed derivative terms (second and third

terms) to vanish. As a result,

$$\left(\frac{\tau}{\mu}\right) \frac{\partial c}{\partial x} \sim D \frac{\partial^3 c}{\partial z^3},$$

from which it follows that the thickness of the concentration boundary layer in the vertical direction scales as  $(D\mu x/\tau)^{1/3}$ . At  $z = 0$ , equation (3.1) also indicates that the lateral and vertical concentration gradients are comparable, which therefore yields the scaling  $\delta(z = 0) \sim (D\mu x/\tau)^{1/3}$ . This scaling behaviour for  $z = 0$  is a direct consequence of the linearity of the velocity profile  $u_x \sim z$  as well as the condition that the vertical concentration flux vanishes at the substrate surface, i.e.  $(\partial c/\partial z)_{z=0} = 0$ . The presence of the  $\frac{1}{3}$  scaling in this system is unrelated to the approximations used for Poiseuille-like velocity profiles in studies of pressure-driven flow in enclosed rectangular microchannels, where  $u_x \sim \text{const.}$  near the central part of the channel and  $u_x \sim z$  near the solid wall (Ismagilov *et al.* 2000; Kamholz & Yager 2001). Additional numerical simulations show that the presence of slip at the liquid–solid interface (i.e.  $u_x(z = 0) \neq 0$ ) generates a scaling closer to  $\delta_{0.3}(z = 0) \sim x^{1/2}$ , since the convective term loses the linear dependence on  $z$ .

As is apparent from a non-dimensionalization of equation (3.1), the mixing length scales as

$$l_{\text{mix}} \sim \frac{u_{\text{max}} w^2}{D} = h_{\text{max}} \frac{\tau w^2}{\mu D},$$

which is confirmed by the numerical solutions. As in the case of stagnant streamlets, the mixing length-scales linearly with the film height  $h_{\text{max}}$  and quadratically with the microstripe width  $w$ . These dependencies are expected since, in the absence of a transverse shear stress, lateral solute transport can only occur by diffusion.

### (c) *Mixing in Y-junctions*

In the previous section it was assumed that the height and velocity profiles were translationally invariant along the  $\hat{x}$ -axis and that the boundary condition corresponded to a sharp interface between adjacent liquid streams. For mixing in Y-junctions, as shown on the left of figure 1*b*, two initially separate streams merge into one. The junction induces a bulge in the liquid interface due to the strong effect of surface tension in geometries with large surface-to-volume ratios. In this section, the actual surface shape is taken into account, which leads to an additional contribution to the velocity profile caused by capillary pressure gradients. The full temperature dependence of the viscosity and diffusivity is also retained. The small aspect ratios,  $(h_{\text{max}}/w)^2 \ll 1$ , allow derivation of a height-averaged convective–diffusive equation, whose solutions are compared with experiment in § 3*f*.

Within the lubrication approximation, the film height is governed by the nonlinear equation (Darhuber *et al.* 2003*a*)

$$\frac{\partial h}{\partial t} + \nabla \cdot \left[ \frac{\gamma_0 h^3}{3\mu} \nabla(\nabla^2 h) + \frac{\tau h^2}{2\mu} \right] = 0. \quad (3.3)$$

Non-dimensionalization of the variables according to  $\xi = x/w$ ,  $\zeta = y/w$ ,  $\tilde{h} = h/h_{\text{max}}$ ,  $\tilde{\mu} = \mu/\mu_0$  and  $\tilde{\tau} \equiv (3w^3\tau)/(2\gamma_0 h_{\text{max}}^2)$  yields the dimensionless form of the steady-

state evolution equation:

$$\tilde{\nabla} \cdot \left( \frac{\tilde{h}^3}{\tilde{\mu}} \tilde{\nabla} \tilde{\nabla}^2 \tilde{h} + \tilde{\tau} \frac{\tilde{h}^2}{\tilde{\mu}} \right) = 0. \quad (3.4)$$

In the numerical simulations the reference values  $h_{\max}$ ,  $\gamma_0$  and  $\mu_0$  were evaluated at the position  $x = 10$  mm downstream of the Y-junction.

Since vertical concentration gradients are small, the concentration field is essentially independent of  $z$ , i.e.  $c = c(x, y, t)$ . In this limit, the form of the species-conservation equation consistent with the lubrication approximation becomes

$$\frac{\partial(hc)}{\partial t} + \nabla \cdot (h\mathbf{N}) = 0, \quad (3.5)$$

where the species flux  $\mathbf{N}$  (e.g. dye flux) is given by

$$\mathbf{N} = -D\nabla c + \frac{1}{h} \int_0^h c\mathbf{V} dz = -D\nabla c + c\mathbf{V}_{\text{avg}} = -D\nabla c + c \left[ -\frac{h^2}{3\mu} \nabla p + \frac{\tau h}{2\mu} \right]. \quad (3.6)$$

Substituting this expression into equation (3.5) yields

$$\frac{\partial(hc)}{\partial t} + \nabla \cdot (hc\mathbf{V}_{\text{avg}}) = \nabla \cdot (Dh\nabla c). \quad (3.7)$$

Noting that

$$\frac{\partial h}{\partial t} + \nabla \cdot (h\mathbf{V}_{\text{avg}}) = 0$$

from equation (3.3), the final form of the species-conservation equation is

$$h \frac{\partial c}{\partial t} + h\mathbf{V}_{\text{avg}} \cdot \nabla c = \nabla \cdot (Dh\nabla c). \quad (3.8)$$

Non-dimensionalization as in equation (3.4) yields the steady-state species-conservation equation,

$$\left( \frac{\tilde{h}^3}{\tilde{\mu}} \tilde{\nabla} \tilde{\nabla}^2 \tilde{h} + \frac{\tilde{\tau} \tilde{h}^2}{\tilde{\mu}} \right) \cdot \tilde{\nabla} \tilde{c} = \tilde{\nabla} \cdot (\tilde{D} \tilde{h} \tilde{\nabla} \tilde{c}), \quad (3.9)$$

where  $\tilde{D} = (3\mu_0 w^2 D)/(\gamma_0 h_{\max}^3)$  is the dimensionless diffusion constant. Using the Stokes–Einstein equation,  $D$  can be re-expressed as  $D_0(T\mu_0)/(T_0\mu)$ , where  $D_0$  is the reference value of the diffusivity evaluated at  $T_0$  and  $\mu_0$ . This expression is incorporated into equation (3.9), which is used to obtain the numerical solutions outlined in §3*f*.

#### (d) Experimental set-up

Samples were prepared from silicon wafers as shown schematically in figure 1*b* and described in detail elsewhere (Darhuber *et al.* 2003*a*). The liquids used in these experiments were pure and dyed polydimethylsiloxane (PDMS) ( $\mu = 18$  mPa s at 21 °C,  $\partial\gamma/\partial T = -6 \times 10^{-5}$  N m<sup>-1</sup>). The surface tension of PDMS, which was unaffected by the low concentration of dye, was measured to be  $\gamma = (19.9 \pm 0.1)$  mN m<sup>-1</sup> at 22 °C. Two 6  $\mu$ l droplets of pure and dyed PDMS were first deposited on the square reservoir sites using a Hamilton digital syringe with a volume resolution of 0.1  $\mu$ l. The dye

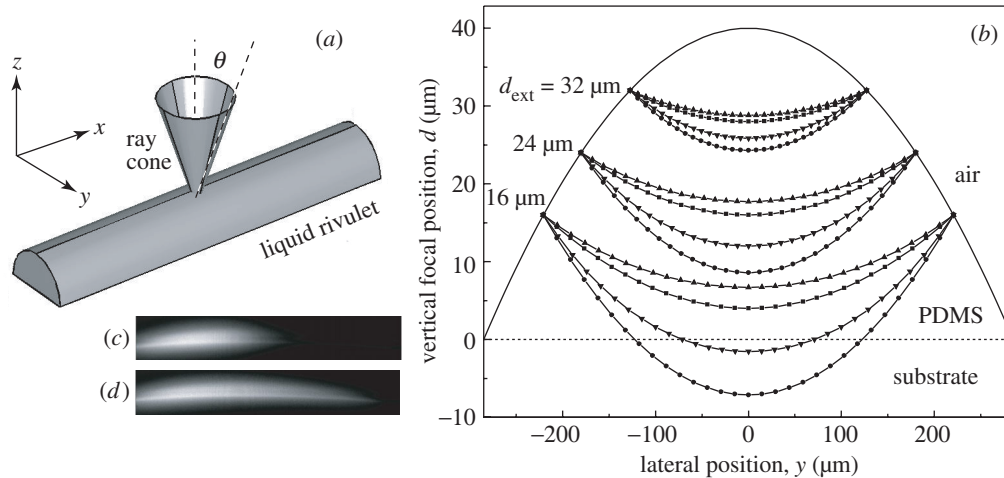


Figure 3. (a) Diagram of the optical beam path for a cone of light with opening angle  $\theta$  focused in the interior of a liquid rivulet. (b) Ray-tracing of light paths within a rivulet with  $h_{\max} = 40 \mu\text{m}$ . Distances  $d_{\text{ext}}$  denote the elevation of the focus point (in air) above the solid surface. The symbols  $\blacktriangle$ ,  $\blacktriangledown$ ,  $\bullet$  and  $\blacksquare$  denote the focal positions of paraxial and large- $\theta$  rays inside the rivulet in the  $\hat{y}$ - $\hat{z}$  and  $\hat{x}$ - $\hat{z}$  coordinate planes, respectively. (c), (d) CFM images in the  $\hat{y}$ - $\hat{z}$  plane recorded in reflection mode on an Si sample at distances (c)  $x = 1 \text{ mm}$  and (d)  $12 \text{ mm}$  downstream of the Y-junction for a rivulet with  $h_{\max} \approx 40 \mu\text{m}$ .

used to track interfacial broadening was Lumogen F Red 300 (BASF), a perylene based fluorescent dye with maximum absorption at a wavelength of  $\lambda = 578 \text{ nm}$  and peak emission at  $\lambda = 613 \text{ nm}$ .<sup>†</sup> A dilute solution was prepared by stirring, ultrasonic agitation and filtering with a  $5 \mu\text{m}$  syringe filter. Local dye concentrations were measured with an MRC-600 confocal microscope (BIO-RAD Laboratories, San Jose, CA, USA) using an Ar-ion laser wavelength of  $568 \text{ nm}$ . Measurements commenced after 45 min in order to establish steady-state conditions.

The optical set-up is shown in figure 3a, b. Under normal operation, the cone of light from a  $20\times$  microscope objective with numerical aperture 0.75 was focused at a height  $d_{\text{ext}}$  above the sample surface. Since the refractive index of PDMS ( $n \approx 1.403$ ) is larger than the refractive index of air ( $n_{\text{air}}$ ), the focal position of the incident light was displaced from its position at the air-liquid interface to a distance  $d$  from the substrate surface. Moreover, paraxial rays focus at different depths from rays with large inclination angles. Since the surface of the liquid rivulet was rather flat in the  $\hat{x}$ -direction but curved in the  $\hat{y}$ -direction, the focus height also depended on the azimuthal plane of incidence of the incident light rays. Figure 3b illustrates the large vertical spread of the focal point inside the liquid rivulet for paraxial and high-angle rays in two perpendicular planes of incidence. The subsequent loss in vertical resolution did not compromise the experiments, since the iso-concentration lines remain rather vertical due to the small aspect ratio  $h_{\max}/w$ . The vertical resolution was, however, insufficient to resolve the  $\delta \sim x^{1/2}$  versus  $\delta \sim x^{1/3}$  scalings discussed in § 3b. The position-dependent downward shift of the focal point inside the liquid film slightly distorted the apparent cross-sectional shape from a parabola to a crescent.

<sup>†</sup> Lumogen F Red product information sheet, BASF Corp. (Rensselaer, NY, USA).

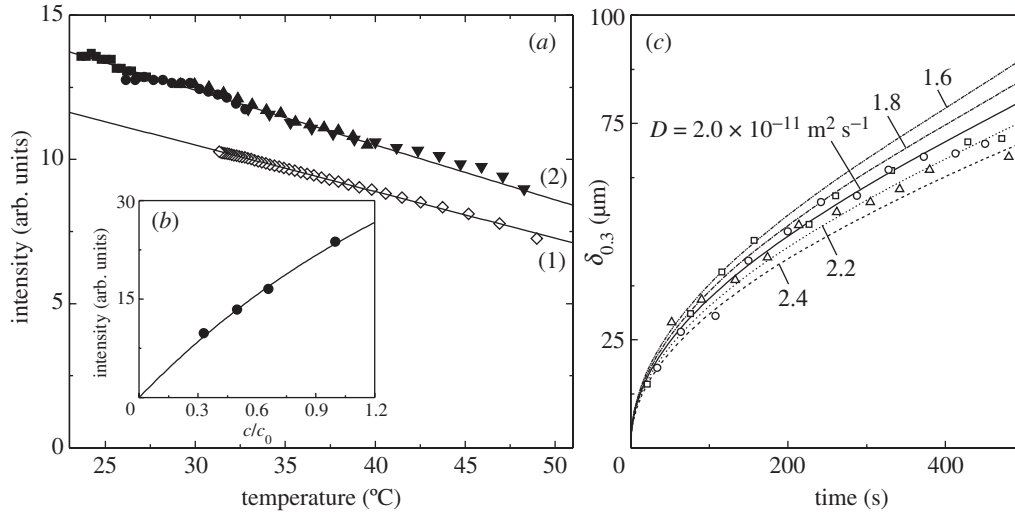


Figure 4. (a) Thermal variation of the fluorescence intensity of Lumogen Red in PDMS (open diamonds). The data are well fitted by a straight (solid) line. The solid symbols represent the integrated intensity of cross-sectional images of dyed and undyed PDMS intermixing on a hydrophilic microstripe for four values of the temperature gradient. The solid fitted lines (1) and (2) have the same relative slope. (b) Fluorescence intensity versus relative dye concentration. The solid line represents the function  $I = A[1 - \exp(-b\tilde{c})]$  with fit-parameters  $A$  and  $b$ . To good approximation, the relation between measured fluorescence intensity and relative dye concentration is linear for the dilutions used. (c) Experimental determination of the diffusion coefficient  $D$  for Lumogen Red in PDMS. Measurements of  $\delta_{0.3}(z \approx h_{\max}/4, t)$  compare favourably with a numerical solution (lines) corresponding to  $D = 2.0 \times 10^{-11} \text{ m}^2 \text{ s}^{-1}$ .

Figure 3*c, d* shows examples in cross-section of two fluorescing rivulets imaged on a silicon sample.

Concentration measurements in non-isothermal systems must account for the thermal dependence of the fluorescence efficiency, as non-radiative vibrational energy transfer becomes more efficient at higher temperatures (Guilbault 1990). The relation between temperature and measured intensity  $I$  is typically linear,

$$\frac{I(T)}{I(T_0)} = 1 - \alpha(T - T_0),$$

with a slope  $\alpha$  between 0.01 and 0.05  $\text{K}^{-1}$ . Measurements of Lumogen Red in PDMS (open diamonds in figure 4*a*) produced values of  $\alpha = (1.65 \pm 0.05) \times 10^{-2} \text{ K}^{-1}$ . This thermal effect was noted to produce a slight but systematic increase of the integrated fluorescence intensity towards the cold side of the substrates. The integrated intensities of cross-sectional CFM images as a function of the local temperature for four consecutive measurements subject to different  $dT/dx$  (solid symbols in figure 4*a*) showed excellent agreement with the expected linear relation. The experimental data for the fluorescence intensities were normalized to a uniform temperature for the analysis below. Figure 4*b* presents the dependence of fluorescence intensity on dye concentration, demonstrating the validity of the linear relation used in extracting the (dilute) dye concentration values from measurements of the fluorescence intensity.

Measurements of the diffusive broadening of the interface separating two adjacent stagnant streams were used to determine the diffusion coefficient of the dye molecules. One dyed and one undyed droplet of liquid were deposited on the two upper square reservoirs of the Y-junction shown on the left of figure 1*b*. A large thermal gradient ( $dT/dx = 11.8 \text{ K cm}^{-1}$ ) was used to flow and merge the liquid streams onto the single microstripe. At  $t = 0$  the heat source was switched off and the sample rapidly cooled to room temperature. CFM was used to measure the lateral broadening of the iso-concentration line corresponding to  $\tilde{c} = 0.3$ . In figure 4*c* three measured datasets of  $\delta_{0.3}(z \approx h_{\text{max}}/2, t)$  are plotted, along with corresponding numerical simulations (lines). The best fit to the data yielded a value  $D = (2 \pm 0.2) \times 10^{-11} \text{ m}^2 \text{ s}^{-1}$ . This was the value of the diffusion coefficient,  $D_0$ , used in computing solutions to equation (3.9).

(*e*) *Design of microstream junctions and bends*

For steady-state conditions, the volumetric flow rate associated with the upper two branches of the Y-junction shown in figure 1*b* must equal the flow rate onto a single stripe, i.e.  $Q_{\text{out}} = 2Q_{\text{in}}$  or equivalently,  $A_{\text{out}}\langle v \rangle_{\text{out}} = 2A_{\text{in}}\langle v \rangle_{\text{in}}$ . Here,  $A = \frac{2}{3}h_{\text{max}}w$  is the cross-sectional area of a rivulet and  $\langle v \rangle$  denotes the average flow speed. Far from any inlets, outlets or junctions, the capillary pressure contribution to the flow is small and the flow velocity is dominated by the thermocapillary stress such that  $v \sim h\tau \cos \phi / \mu$ , where  $\phi$  is the angle between the channel and the direction of  $\nabla T$  (see figure 1*b*). The ratio of stripe widths necessary to satisfy steady-state flow becomes  $w_{\text{out}}h_{\text{out}}^2 = 2w_{\text{in}}h_{\text{in}}^2 \cos \phi$ .

The cross-sectional shape of the liquid rivulets forms an arc of a circle because of the chemical patterning used for lateral confinement of the flowing stream. The lateral curvature of the stream therefore scales as  $h_{\text{max}}/w^2$  (Darhuber *et al.* 2001). For thermocapillary stresses to dominate the flow, it is required that capillary pressure gradients be vanishingly small, since otherwise a pooling of liquid and corresponding recirculatory flow would occur near regions of high surface curvature. For a long rivulet,  $p = \gamma/R$ , where  $R$  is the transverse radius of curvature of the air–liquid interface. Since  $1/R$  scales as  $h_{\text{max}}/w^2$ , the imposed condition of constant pressure throughout is equivalent to  $h_{\text{in}}/w_{\text{in}}^2 = h_{\text{out}}/w_{\text{out}}^2$ . Substituting this second condition into the first gives  $w_{\text{out}} = w_{\text{in}}\sqrt[5]{2 \cos \phi}$ . For the experiments described here, the stripe widths and bend angle were chosen to be  $w_{\text{in}} = 500 \mu\text{m}$ ,  $\phi = 15^\circ$  and  $w_{\text{out}} \approx 570 \mu\text{m}$ . For the case of flow along a simple bend whose microstripe is oriented at an angle  $\varphi$  with respect to  $\nabla T$  (see pattern to the right of figure 1*b*), the analogous argument leads to the relation  $w_{\text{out}} = w_{\text{in}}/\sqrt[5]{\cos \varphi}$ .

(*f*) *Comparison of numerical solutions with experimental data*

Equations (3.4) and (3.9) were solved numerically using triangular finite elements with linear basis functions and parameter values for the film thickness, shear stress, viscosity and diffusion coefficient derived from experiment. Polynomial fits to measurements of the variation of surface tension and viscosity with temperature yielded the following:  $\gamma(T)$  ( $\text{mN m}^{-1}$ ) =  $21.5 - 0.06T$  ( $^\circ\text{C}$ ) and  $\mu(T)$  ( $\text{mPa s}$ ) =  $27.676 - 0.316T - 0.0032T^2 + 8.882 \times 10^{-5}T^3$ . Solution convergence and accuracy were checked through mesh refinement and the use of a cubic basis, which produced the same result as the linear basis. Equation (3.4) was first solved with a

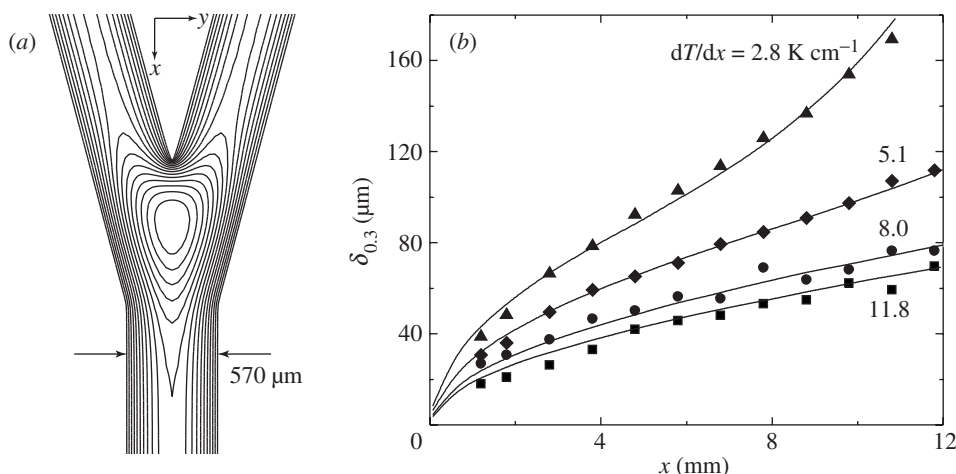


Figure 5. (a) Contour plot of the numerical solutions for the liquid height profile  $h(x, y)$  in the vicinity of the Y-junction. The local maximum in  $h(x, y)$  at the junction is *ca.* 55% higher than the downstream value of  $h_{\max}$ . (b) Comparison of the measured interfacial diffusive broadening,  $\delta_{0.3}(x)$ , with full numerical solutions of the height-averaged concentration field including the temperature variation of  $\mu$  and  $D$ . The experimental values were extracted from cross-sectional CFM images at a distance from the solid surface  $z \approx h_{\max}/4$ .

nonlinear solver using Newton's method and an estimate for  $h_{\max}$  (which could be obtained experimentally within  $\pm 5 \mu\text{m}$ ). The boundary conditions specified the value of  $h_{\max}$  at the inlets of the two converging streams with vanishing film height at the microstripe edges. The computed film shape  $h(x, y)$  was used to solve equation (3.9) using a linear solver based on Gaussian elimination. The dimensionless concentration was set to unity at the inlet of one microstream and zero at the inlet of the other. A no-flux condition was imposed at all lateral boundaries. This procedure was repeated for different values of  $h_{\max}$  until the best match with experimental measurements was obtained.

The free surface shape of the liquid streams is shown in figure 5a for  $\tau_x = 0.017 \text{ Pa}$  and  $\tau_y = 0$ . Profiles for other parameter values were qualitatively similar. A pronounced liquid bulge appears at the junction of the two microstrips where the maximum height is *ca.* 50% larger than the downstream value of  $h_{\max}$ . This accumulation of liquid is due to capillary effects and decreases slightly as  $\tau_x$  increases. The local film height increases here and the flow speed is reduced, which locally enhances diffusive mixing at the junction position.

This free surface shape was then used to compute the steady-state dye concentration profile for a dye molecular diffusivity value of  $D = 2.0 \times 10^{-11} \text{ m}^2 \text{ s}^{-1}$ . Measured values of  $\delta_{0.3}(x)$  for values of thermal gradient  $dT/dx = 11.8, 8.0, 5.1$  and  $2.8 \text{ K cm}^{-1}$  are plotted in figure 5b. The reference heights that provided the best fit to the experimental data were determined to be  $h_{\max} = 40, 40, 39,$  and  $44 \mu\text{m}$ , respectively. The agreement with experiment is generally very good and the expected  $\delta \sim x^{1/2}$  scaling is reproduced well. The steepening of  $\delta_{0.3}(x)$  visible at  $x \geq 8 \text{ mm}$  for the lowest gradient is a finite size effect. It occurs when  $\delta_{0.3}$  becomes comparable with  $w/2$ , at which point the curve  $\delta_{0.3}(x)$  terminates as described in § 3 b.

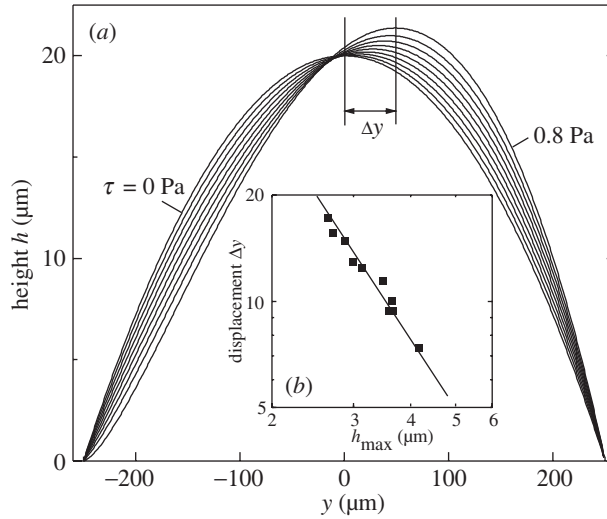


Figure 6. (a) Steady-state rivulet height profiles for  $w = 500 \mu\text{m}$  and  $\tau$  ranging from 0 to 0.8 Pa in increments of 0.1 Pa. The apex point of the rivulet is displaced towards the cooler side with increasing  $\tau = |\tau_{zy}|$ . (b) Variation in apex displacement,  $\Delta y$ , with increasing  $h_{\text{max}}$  for  $w = 300 \mu\text{m}$  and  $\tau = 0.065 \text{ Pa}$ . The solid line corresponds to a power law  $\Delta y \sim h_{\text{max}}^{-2}$ .

#### 4. Active mixing by constant transverse thermal gradients

Application of a thermal gradient perpendicular to a rivulet constitutes another method for mixing initially separate liquid volumes. Since the chemical patterning pins the contact lines at the liquid edges, application of a purely transverse gradient  $|\nabla T| = \partial T / \partial y$  creates a convective flow as sketched in figure 1c. As shown below, this convection pattern establishes a progressive lamination of the two liquid samples, which provides a very efficient means for reducing the mixing time. In this case, the mixing time is not determined by the large lateral length-scale  $w$  but rather by the much shorter vertical length-scale  $h_{\text{max}}$ .

##### (a) Distortion of rivulet shape

Since the liquid stream cannot migrate onto the non-wetting portions of the substrate, the volumetric flux in the  $\hat{y}$ -direction, due to a constant transverse thermocapillary stress, must vanish under steady-state conditions. For a rivulet shape that is translationally invariant along the  $\hat{x}$ -axis, this no-flux condition produces the required equation governing the distortion in film height:

$$\frac{h^2 \tau_{zy}}{2\mu} - \frac{h^3}{3\mu} \frac{\partial p}{\partial y} = 0 \quad \Rightarrow \quad \tilde{h} \frac{\partial^3 \tilde{h}}{\partial \tilde{y}^3} = -\frac{3\tau_{zy} w^3}{16\gamma h_{\text{max}}^2}. \quad (4.1)$$

For  $\tau_{zy} = 0$ , the solution  $\tilde{h}(\tilde{y}) = (1 - \tilde{y}^2)$  is a parabola which is symmetric about the centre of the microstripe. For  $\tau_{zy} \neq 0$ ,  $\tilde{h}(\tilde{y})$  assumes an asymmetric shape, since the liquid centre of mass is shifted towards the cooler side. Numerical solutions for the distortion in height profile for different values of the shear stress  $|\boldsymbol{\tau}| = \tau_{zy}$  are presented in figure 6a. Measurements of the shape distortion, by optical interferometry for instance, can therefore provide a unique way of accurately measuring temperature gradients on a solid surface. Figure 6b presents experimental data for  $\Delta y$  as a

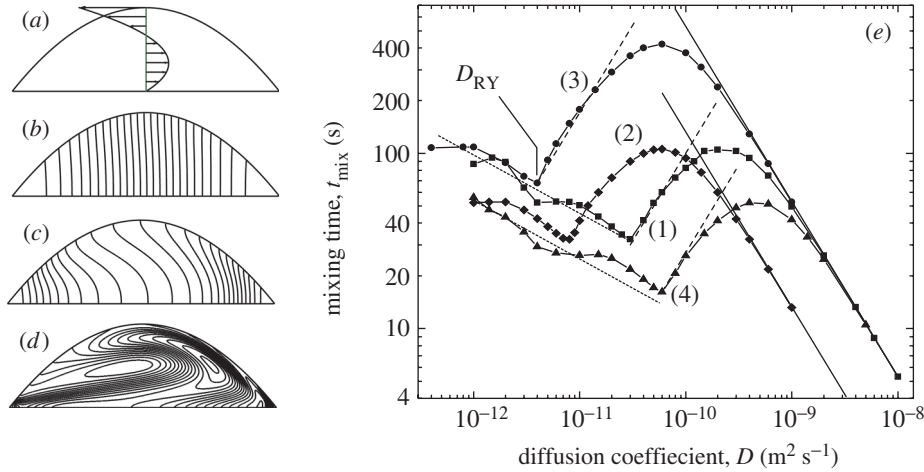


Figure 7. (a) Velocity profile  $u_x(y = 0, z)$  induced by a purely transverse temperature gradient  $dT/dy > 0$ . (b)–(d) Iso-concentration contour lines at  $t = t_{\text{mix}}$  for  $w = 600 \mu\text{m}$ ,  $h_{\text{max}} = 50 \mu\text{m}$ ,  $\tau = 0.1 \text{ Pa}$  and (b)  $D = 2 \times 10^{-9} \text{ m}^2 \text{ s}^{-1}$ , (c)  $D = 1 \times 10^{-10} \text{ m}^2 \text{ s}^{-1}$ , and (d)  $D = 2 \times 10^{-12} \text{ m}^2 \text{ s}^{-1}$ . (e) Mixing time  $t_{\text{mix}}(D)$  for  $h_{\text{max}} = 50 \mu\text{m}$ ,  $w = 600 \mu\text{m}$  and  $\tau = 0.1 \text{ Pa}$  (curve (1), squares). Curve (3) (circles):  $h_{\text{max}}$  was decreased to  $25 \mu\text{m}$ , other parameters unchanged. Curve (4) (triangles):  $\tau$  was increased to  $0.2 \text{ Pa}$ , other parameters unchanged. Curve (2) (diamonds):  $h_{\text{max}} = 25 \mu\text{m}$ ,  $w = 300 \mu\text{m}$  and  $\tau$  unchanged. The data for large  $D$  are reproduced well by the purely diffusive relation  $t_{\text{mix}} \sim D^{-1}$  (solid lines). The dashed and dotted lines correspond to power-law relations  $t_{\text{mix}} \sim D$  (i.e.  $Pe^{-1}$ , TA regime) and  $t_{\text{mix}} \sim D^{-1/3}$  (i.e.  $Pe^{1/3}$ , RY regime), respectively.

function of  $h_{\text{max}}$  for  $w = 300 \mu\text{m}$  and  $\tau = 0.065 \text{ Pa}$ . The solid line corresponds to the power law  $\Delta y \sim h_{\text{max}}^{-2}$ . The slight scatter in the data is due to small unintentional temperature gradients along the  $\hat{x}$ -axis, which modulated the local rivulet height as the temperature gradient was switched on. For the metrology of surface temperature gradients, it is therefore preferable to measure apex displacements of liquids on small circular pads.

The dimensional lateral velocity field  $u_y(y, z)$  for this configuration is given by (Darhuber *et al.* 2003a)

$$u_y = \frac{\tau}{\mu} z + \frac{1}{\mu} \frac{\partial p}{\partial y} \left( \frac{z^2}{2} - hz \right) = \frac{h\tau}{4\mu} \left( \frac{3z^2}{h^2} - \frac{2z}{h} \right), \quad (4.2)$$

which shows the existence of a stagnation point at  $z = 2h(y)/3$  (see figure 7a). The presence of capillary backflow causes a reduction in the surface velocity to  $1/4$  the value it would have were the same shear stress applied to a flat thin liquid layer. Integration of the continuity equation  $\nabla \cdot \mathbf{u} = 0$  determines the vertical velocity component, namely

$$u_z = - \int_0^z \frac{\partial u_y}{\partial y} dz = \frac{h\tau}{4\mu} \frac{z^3}{h^3} \frac{\partial h}{\partial y} \ll u_x. \quad (4.3)$$

As expected within the lubrication approximation,  $\tilde{u}_z/\tilde{u}_{\tilde{y}}$  is of order  $h_{\text{max}}/w$ .

(b) *Mixing with a purely transverse shear stress*

Substitution of the velocity field  $\mathbf{u} = (0, u_y, u_z)$ , the streamlines of which are sketched in figure 1c, into equation (2.1) leads to a solution of the concentration field  $c(y, z, t)$ . The viscosity and diffusion coefficient are assumed temperature independent since the characteristic scale along the  $\hat{y}$ -axis is rather small i.e.  $w = 500 \mu\text{m}$ . In the absence of any lateral convection, the diffusive mixing time is of order  $4 \times 10^4 \text{ s}$  (11 h) for  $D = 1.0 \times 10^{-12} \text{ m}^2 \text{ s}^{-1}$ . Application of a constant thermocapillary stress  $\tau_{zy}$  leads to flow lamination which increases the interfacial area between two liquid samples essentially linearly in time. For a thermal gradient of  $dT/dy = 4 \text{ K mm}^{-1}$  and liquid viscosity  $\mu = 0.02 \text{ Pa s}$ , the interfacial area increases by a factor of 50 within 10 s. The mixing is rather rapid throughout the rivulet centre portion with longer equilibration times in the tapered corners. The presence of convective flow decreases the mixing time to *ca.* 30 s, which is three orders of magnitude less than mixing by pure diffusion for this specific example.

The relative reduction of the mixing time  $t_{\text{mix}}$  compared with purely diffusive mixing depends strongly on the value of  $D$  in a non-trivial manner. Figure 7b–d depicts the iso-concentration lines for fixed values of  $h_{\text{max}}$ ,  $w$  and  $\tau_{zy}$  and decreasing values of the diffusion coefficient. In figure 7e the mixing time  $t_{\text{mix}}$  is plotted as a function of  $D$  for various parameter values  $h_{\text{max}}$ ,  $w$  and  $\tau$ . Three distinct regimes are evident. For large values of  $D$  (diffusive regime), the convective flow induces only a minor perturbation to the concentration field such that the mixing time-scales as  $t_{\text{mix}} \sim w^2 D^{-1}$ . As shown in figure 7b, the iso-concentration lines are only slightly displaced from the position expected for purely diffusive mixing along the  $y$ -axis. The numerical solutions in the limit of large  $D$  confirm this scaling, as shown by the solid lines in figure 7e.

Rhines & Young (1983) previously studied the homogenization of a passive tracer in a shear flow with closed streamlines. Applying their result for the convection-dominated regime directly to this example would predict that

$$t_{\text{mix}} \sim \left(\frac{\mu}{\tau}\right) \left(\frac{w}{h_{\text{max}}}\right) Pe_w^{1/3}$$

(i.e.  $t_{\text{mix}} \sim D^{-1/3}$  for small  $D$  and large values of the Péclet number  $Pe_w = h_{\text{max}}\tau w/\mu D$ ). As shown in figure 7d, the iso-concentration lines in this regime are strongly distorted such that the most significant gradients in concentration occur along the vertical and not the horizontal direction. The Rhines & Young (RY) scaling can be understood by examining the dominant terms in equation (2.1):

$$\frac{\partial c}{\partial t} + u_y \frac{\partial c}{\partial y} = D \frac{\partial^2 c}{\partial z^2}. \quad (4.4)$$

Balancing the two terms representing transverse convection and vertical diffusion yields the relation  $h_{\text{max}}^3 \sim \mu w D/\tau$ . Substitution of this scaling into the time-scale associated with vertical diffusion,  $h_{\text{max}}^2/D$ , produces an estimate of the mixing time for shear-augmented diffusion in the strong convection limit, namely

$$t_{\text{mix}} \sim \left(\frac{\mu}{\tau}\right) \left(\frac{w}{h_{\text{max}}}\right)^{1/3} Pe_w^{1/3}.$$

The exponent of the ratio  $w/h_{\max}$  is reduced to  $1/3$  because of the small geometric aspect ratio. This expression also shows that the mixing time for a system that is isotropically inflated  $(h, w) \rightarrow (\alpha h, \alpha w)$  is equivalent to that of the original system with  $D \rightarrow D/\alpha^2$ . The numerical solutions shown by the short-dashed lines in figure 7e generally follow the scaling  $t_{\text{mix}} \sim D^{-1/3}$ . The oscillations in  $t_{\text{mix}}(D)$  are due to (decaying) modulations in  $K(t)$ . The RY regime terminates when the time-scale for vertical diffusion is equal to the convective time-scale, i.e. for a value of the diffusion constant  $D_{\text{RY}} \sim h_{\max}^3 \tau / (\mu w)$ . This transition is shown in figure 7e; changes in the parameters  $h_{\max}$ ,  $\tau$  and  $w$  by a factor of 2 affect the crossover position  $D_{\text{RY}}$  by factors of 8, 2 and 2, respectively.

Taylor (1953) and Aris (1956) showed long ago that the dispersion of solute flowing in a circular tube of radius  $a$  could be described by an effective diffusivity  $D_{\text{eff}} = D + a^2 U^2 / (48D)$ , where  $U$  is the characteristic velocity. In our system, a Taylor–Aris-like (TA-like) regime can develop for intermediate values of  $D$ , such that  $t_{\text{mix}} \sim D$ . In this case, contrary to intuition, an increase in  $D$  leads to an increase in  $t_{\text{mix}}$  thereby *decreasing* the mixing efficiency. The long-dashed lines in figure 7e correspond to the linear relation  $t_{\text{mix}} \sim D$ . The numerical solutions in this crossover regime are represented well by this linear scaling. Moreover, a comparison of the numerical solutions in this regime shows a quadratic dependence on  $\tau \sim u_{\max}$  as should occur for dispersion effects. Figure 7c illustrates the distortion of the iso-concentration lines in the TA regime. The existence of this regime is caused directly by the small geometric aspect ratio  $h_{\max}/w$  in these systems.

For a given set of parameters  $w$ ,  $h_{\max}$  and  $\tau$  and the mixing criterion  $K < 0.05$ , there exists a local minimum in the mixing time for a diffusion coefficient  $D = D_{\text{RY}}$ . Conversely, for a specific combination of solute and solvent with a given diffusion constant  $D$ , there exists an optimal value of  $h_{\max}$  for which mixing occurs more rapidly. In general, reducing  $w$  or increasing  $\tau$  leads to a decrease in  $t_{\text{mix}}$ .

## 5. Active mixing by vortex pairs

As sketched in figure 1c, the application of a constant transverse temperature gradient produces a single convection cell in the centre of the rivulet. Qualitatively different convection patterns can be established by engineering the substrate surface temperature. In figure 8a, for example, a microheater embedded beneath the substrate surface generates a local temperature maximum at  $y = 0$  and cooler temperature at the sides of the rivulet. In figure 8b, a thin substrate of moderate thermal conductivity  $k$  (e.g. glass) operated above room temperature and positioned on top of a slotted metal plate exposes the rivulet to convective air cooling. The surface temperature  $T(y)$  is therefore lower in the centre and higher at the edges.

For both geometries the temperature distribution is symmetric,  $T(y) = T(-y)$ , resulting in a mirror-symmetric velocity field. Two important differences with respect to the single-vortex case considered earlier are that the velocity field is perpendicular to the concentration gradient at  $t = 0$  and that mass transfer across the plane  $y = 0$  occurs only by diffusion. The convective flow, therefore, does not induce the type of lamination observed within a single convection cell; it merely accelerates the concentration equilibration within the left and right sides of the rivulet. To illustrate the influence of such symmetric convection patterns on  $t_{\text{mix}}$ , the thermal field is approximated by  $T(y) \approx T_0 + \delta T(1 - 4y^2/w^2)$ . It is assumed that the thermocapillary stress

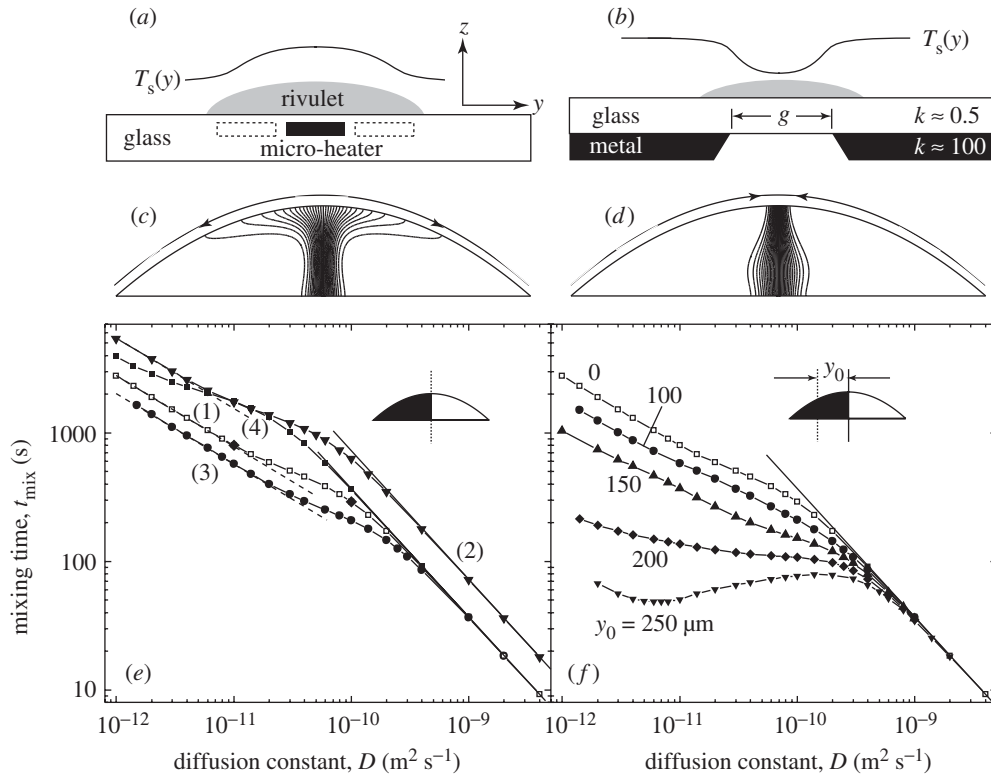


Figure 8. (a) Cross-section of a rivulet on a substrate with a microheater embedded underneath the hydrophilic microstripe. This configuration generates two adjacent convective cells. The dashed rectangles indicate possible off-centre heater locations. (b) Cross-section of a glass substrate attached to a metal plate with a slot underneath the hydrophilic channel. Due to convective and radiative cooling, the temperature on the glass surface  $T_s(y)$  above the slit is reduced. This configuration also generates two adjacent convective cells. (c), (d) Iso-concentration contour lines at time  $t = 10$  s for thermocapillary mixing due to a parabolic temperature profile  $T_s(y) = T_0 + \delta T(1 - 4y^2/w^2)$ . The parameter values are  $\delta T = \pm 0.125$  K,  $w = 500$   $\mu\text{m}$ ,  $h_c = 50$   $\mu\text{m}$  and  $\mu = 0.02$  Pa s. (e) Mixing time  $t_{\text{mix}}(D)$  for  $w = 500$   $\mu\text{m}$ ,  $h_{\text{max}} = 50$   $\mu\text{m}$  and  $\delta T = 0.125$  K (open circles, curve (1)). The other curves represent the change of a single parameter with respect to (1). Curve (2) (triangles):  $w = 700$   $\mu\text{m}$ . Curve (3) (filled circles):  $\delta T = 0.25$  K. Curve (4) (squares):  $h_{\text{max}} = 25$   $\mu\text{m}$ . The diamonds correspond to  $\delta T = -0.125$  K. (f) Mixing time  $t_{\text{mix}}(D)$  for  $w = 500$   $\mu\text{m}$ ,  $h_{\text{max}} = 50$   $\mu\text{m}$  and  $\delta T = 0.125$  K and different displacements,  $y_0$ , of the temperature profile.

is sufficiently small so that the rivulet shape remains parabolic. As time proceeds, the iso-concentration lines near the liquid interface  $z = h(y)$  are either splayed outwards for a diverging velocity field ( $\delta T > 0$ , figure 8c) or compressed inwards by a converging velocity field ( $\delta T < 0$ ) as shown in figure 8d.

The transverse velocity  $u_y$  is given by equation (4.2); however, the vertical component,  $u_z$ , contains an additional contribution,

$$u_z = \frac{3}{4\mu} \frac{\partial \gamma}{\partial T} \left[ \frac{\partial T}{\partial y} \frac{\partial h}{\partial y} \frac{z^3}{3h^2} - \frac{\partial^2 T}{\partial y^2} \left( \frac{z^3}{3h} - \frac{z^2}{3} \right) \right], \quad (5.1)$$

owing to the fact that  $dT/dy$  is not constant. Equation (5.1) reduces to equation (4.3) for constant  $\tau$ .

In figure 8c are plotted curves of  $t_{\text{mix}}(D)$  for different values of  $w$ ,  $h_{\text{max}}$  and  $\delta T$ . The value of  $\delta T = 0.125$  K was chosen to facilitate comparison with the numerical results in § 4, i.e.  $dT/dy(y = w/2) = 1$  K mm<sup>-1</sup>. As before, in the diffusive regime (for large values of  $D$ ),  $t_{\text{mix}}$  scales as  $w^2/D$ . In the convection-dominated regime (small  $D$ ), the circulation patterns enhance mixing and  $t_{\text{mix}}$  is reduced below the value for purely diffusive mixing. Unlike the single vortex case, however, no local minimum in  $t_{\text{mix}}(D)$  is observed. Moreover, the dependence of  $t_{\text{mix}}$  on  $D$  is significantly steeper than the  $D^{-1/3}$  RY scaling: the dashed lines in figure 8e correspond to a fit  $t_{\text{mix}} \sim D^{-0.55}$ . Since the regions enclosed by the streamlines of the vortical flow do not contain concentration gradients initially, the RY and TA regimes described in the previous section are absent in these configurations.

Figure 8f demonstrates the behaviour of  $t_{\text{mix}}(D)$  for a temperature distribution that is displaced from the centre of the rivulet according to  $T(y) = T_0 + \delta T[1 - 4(y - y_0)^2/w^2]$ . In this case, lamination occurs in one section of the rivulet but not in the other. As the position  $y_0$  is moved farther toward the edges of the rivulet and beyond, the mixing time is significantly reduced and the curves  $t_{\text{mix}}(D)$  increasingly resemble the solutions presented in figure 7e.

The mixing efficiency of the double vortex geometry is significantly smaller than that for a single vortex induced by a constant transverse temperature gradient. The salient feature of fast mixing, therefore, appears to be a (non-uniform) velocity field parallel to  $\nabla c$  such that a lamination of the two phases to be mixed can occur. For large  $Pe$ ,  $\nabla c$  becomes more and more perpendicular to  $\mathbf{u}$  (figure 7d). An expedient mixing strategy might therefore be a two-stage process. A single vortex can first be used to distribute the two liquids equally between the left and right sides of the rivulet. A vortex pair can then be generated until complete mixing is achieved.

## 6. Combined longitudinal and transverse gradients

When the microstripe direction is inclined with respect to  $\nabla T$  by an angle  $\varphi$  (see figure 1b), there exists both a longitudinal temperature gradient and a transverse temperature gradient across the rivulet. It is here assumed as before that diffusional transport along  $\hat{x}$  can be ignored and that the rivulet has a parabolic cross-section with constant maximum height  $h_{\text{max}}$ . Within the lubrication approximation, the momentum equations are linear and the velocity field is simply a superposition of the flow fields corresponding to streamwise and transverse thermal gradients, namely

$$u_x = \frac{\tau \cos \varphi}{\mu} z, \quad u_y = \frac{3\tau \sin \varphi}{4\mu} \left[ \frac{z}{h} - \frac{2}{3} \right] z, \quad u_z = \frac{h\tau \sin \varphi}{4\mu} \frac{\partial h}{\partial y} \frac{z^3}{h^3}. \quad (6.1)$$

Both the longitudinal and transverse velocity components are linearly proportional to the respective components of  $\nabla T$ . The streamlines of the resulting helical flow (see the sketch in figure 9a) depend on  $\varphi$  but not  $|\nabla T|$ . Figure 9b shows a comparison of the mixing length  $l_{\text{mix}}(h_{\text{max}})$  for different values of  $\varphi$  and  $D$ . For small  $h_{\text{max}}$ , the mixing is diffusion dominated so that the mixing length is essentially equal to

$$\langle u_x \rangle t_{\text{mix}} \sim \left( \frac{h_{\text{max}} \tau}{\mu} \cos \varphi \right) \left( \frac{w^2}{D} \right).$$

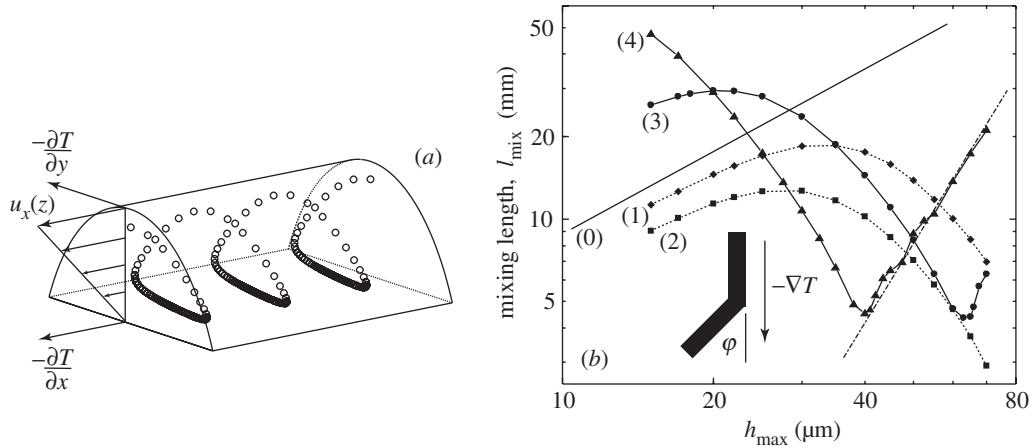


Figure 9. (a) Three-dimensional sketch of helical streamlines in a rivulet which is inclined with respect to the direction of the temperature gradient  $-\nabla T$ . (b) Mixing length  $l_{\text{mix}}$  as a function of  $h_{\text{max}}$  for different values of the rivulet inclination  $\varphi$  and diffusion constant  $D$ . The rivulet width  $w$  and the thermocapillary stress  $\tau$  were held fixed at  $600 \mu\text{m}$  and  $0.1 \text{ Pa}$ , respectively. The curve labelled (0) corresponds to the passive mixing geometry studied in §3. The dash-dotted line corresponds to a power-law relation  $l_{\text{mix}} \sim h_{\text{max}}^3$ . Curve (0),  $\varphi = 0^\circ$ ,  $D = 1.0 \times 10^{-10} \text{ m}^2 \text{ s}^{-1}$ ; curve (1),  $\varphi = 30^\circ$ ,  $D = 1.0 \times 10^{-10} \text{ m}^2 \text{ s}^{-1}$ ; curve (2),  $\varphi = 45^\circ$ ,  $D = 1.0 \times 10^{-10} \text{ m}^2 \text{ s}^{-1}$ ; curve (3),  $\varphi = 30^\circ$ ,  $D = 4.0 \times 10^{-11} \text{ m}^2 \text{ s}^{-1}$ ; curve (4),  $\varphi = 30^\circ$ ,  $D = 1.0 \times 10^{-11} \text{ m}^2 \text{ s}^{-1}$ .

For larger values of  $h_{\text{max}}$ , the TA regime discussed earlier governs the mixing process and  $l_{\text{mix}}$  decreases with increasing  $h_{\text{max}}$ . For even larger values of  $h_{\text{max}}$ ,  $Pe_w$  falls into the RY regime and  $l_{\text{mix}}$  again increases with increasing  $h_{\text{max}}$ . The rate-limiting step in the RY regime is the diffusional flux in the vertical direction. Retaining the two dominant terms in equation (2.1) gives

$$u_x \frac{\partial c}{\partial x} = D \frac{\partial^2 c}{\partial z^2} \iff \frac{u_{\text{max}}}{l_{\text{mix}}} \tilde{u}_{\tilde{x}} \frac{\partial \tilde{c}}{\partial \tilde{x}} = \frac{D}{h_{\text{max}}^2} \frac{\partial^2 \tilde{c}}{\partial \tilde{z}^2}. \quad (6.2)$$

Equation (6.2) indicates that in this regime  $l_{\text{mix}}$  scales as  $h_{\text{max}}^2 u_{\text{max}}/D \sim h_{\text{max}}^3 \tau/\mu D$ . The dash-dotted line in figure 9b corresponds to the power law  $l_{\text{mix}} \sim h_{\text{max}}^3$ , which is an excellent approximation to curve (4) for  $h_{\text{max}}$  exceeding  $40 \mu\text{m}$ . Moreover, according to the relation  $l_{\text{mix}} \sim h_{\text{max}}^3/D$ , the RY segments of curves (3) and (4) should be shifted by a factor of  $\sqrt[3]{4} \approx 1.59$  along the horizontal axis, which is indeed the case.

In contrast to passive mixing with streamwise gradients (§3), generation of helical pathlines through the introduction of streamwise and lateral thermal gradients produces much higher mixing efficiency. The value of  $l_{\text{mix}}$  at the location of the minimum in curve (4) is about a factor of 75 smaller than the corresponding value for purely passive mixing. In addition, there are two values of  $h_{\text{max}}$  (in a range relevant to our experiments) for which  $l_{\text{mix}}$  remains constant for small changes in  $h_{\text{max}}$ , an advantageous feature for technological applications.

## 7. Summary and conclusions

Microfluidic actuation based on modulation of interfacial energies through electrostatic (Pollack *et al.* 2000; Cho *et al.* 2003) or thermal means (Kataoka & Troian

1999; Darhuber *et al.* 2003a, b) has recently been made possible by the integration of actuation mechanisms with chemical patterning of the supporting substrate. In this work, mixing behaviour in continuous mode streaming of microrivulets convected by thermocapillary stresses is investigated within the lubrication approximation. Various configurations conducive to diffusive and convective mixing of adjacent liquid streams are explored by application of thermal gradients parallel and perpendicular to liquid microstreams. Measurements by confocal fluorescence microscopy of the diffusive interfacial broadening in adjacent flowing streams confirm numerical predictions. Insights gained from this study of ‘passive’ mixing are used to probe geometries and configurations suited to ‘active’ mixing methods with short mixing times or reduced mixing lengths. A study of adjacent microstreams subject to transverse thermal stresses, which generate a single vortex flow pattern, demonstrates the existence of three distinct mixing regimes depending on the relative magnitude of convective and diffusive transport. Small Péclet numbers  $Pe_w$ , as expected, lead to purely diffusive behaviour where  $t_{\text{mix}} \sim w^2 D^{-1}$ . Large Péclet numbers give rise to shear-augmented mixing where

$$t_{\text{mix}} \sim \left(\frac{\mu}{\tau}\right) \left(\frac{w}{h_{\text{max}}}\right)^{1/3} Pe_w^{1/3}$$

(or equivalently  $t_{\text{mix}} \sim D^{-1/3}$ ). For intermediate values of  $Pe_w$ , scaling arguments and numerical simulations confirm a third regime characteristic of Taylor–Aris-type dispersion. Dispersion effects lead to a pronounced minimum in the mixing time, which can be several orders of magnitude smaller than the value corresponding to purely diffusive mixing. Scaling arguments are used to determine the value of  $D$  at which the transition in regimes occurs: the predictions agree very well with full numerical simulations.

Thermal fields which generate convective vortex pairs are also investigated. In this case, the lamination of the two phases to be mixed, which was obtained with a single vortex, is no longer possible and the mixing efficiency is reduced. Efficient mixing therefore requires a non-uniform velocity field parallel to the concentration gradient  $\nabla c$  for lamination to occur. For a time-invariant velocity distribution  $\mathbf{u}$  and large Péclet numbers,  $\nabla c$  tends to become more and more perpendicular to  $\mathbf{u}$  as time progresses. Expedient mixing strategies for the fluidic device considered may, therefore, necessitate a two-stage process whereby a single vortex is first used to distribute the two liquids equally between the left and right sides of the rivulet and a vortex pair is then generated to achieve complete mixing. It is hoped that insight gained from these studies can be used to further explore mixing strategies involving discrete droplets as well as more complex actuation schemes, based on spatial and temporal modulation of the velocity field.

This work was supported by grants from the National Science Foundation (CTS and DMR divisions), the National Aeronautics and Space Agency, US Army TACOM-ARDEC, Unilever Research US and the New Jersey Commission on Science and Technology. J.M.D. also kindly acknowledges support from an NDSEG fellowship.

## References

Aris, R. 1956 On the dispersion of a solute in a fluid flowing through a tube. *Proc. R. Soc. Lond.* A **235**, 67–77.

*Phil. Trans. R. Soc. Lond.* A (2004)

- Cho, S. K., Moon, H. & Kim, C.-J. 2003 Creating, transporting, cutting, and merging liquid droplets by electrowetting-based actuation for digital microfluidic circuits. *J. MEMS* **12**, 70–80.
- Darhuber, A. A., Troian, S. M. & Reisner, W. W. 2001 Dynamics of capillary spreading along hydrophilic microstripes. *Phys. Rev. E* **64**, 031603.
- Darhuber, A. A., Davis, J. M., Troian, S. M. & Reisner, W. W. 2003a Thermocapillary actuation of liquid flow on chemically patterned surfaces. *Phys. Fluids* **15**, 1295–1304.
- Darhuber, A. A., Valentino, J. P., Troian, S. M. & Wagner, S. 2003b Thermocapillary actuation of droplets on chemically patterned surfaces by programmable microheater arrays. *J. MEMS* **12**, 873–879.
- Davis, J. M., Fischer, B. J. & Troian, S. M. 2003 A general approach to the linear stability of thin spreading films. In *Interfacial fluid dynamics and transport processes* (ed. R. Narayanan & D. Schwabe). Lecture Notes in Physics, vol. 628, pp. 79–106. Springer.
- Deen, W. M. 1998 *Analysis of transport phenomena*. Oxford University Press.
- Deshmukh, A. & Liepmann, D. 2000 Continuous microfluidic mixing using pulsatile micropumps. *Bull. Am. Phys. Soc.* **45**, 137.
- Golovin, A. A., Rubinstein, B. Y. & Pismen, L. M. 2001 Effect of van der Waals interactions on the fingering instability of thermally driven thin wetting films. *Langmuir* **17**, 3930–3936.
- Grigoriev, R. O. 2003 Contact line instability and pattern selection in thermally driven liquid films. *Phys. Fluids* **15**, 1363–1374.
- Guilbault, G. G. (ed.) 1990 *Practical fluorescence*. New York: Marcel Dekker.
- Handique, K. & Burns, M. A. 2001 Mathematical modeling of drop mixing in a slit-type microchannel. *J. Micromech. Microengng* **11**, 548–554.
- Hitt, D. L. & Lowe, M. L. 1999 Confocal imaging of flows in artificial venular bifurcations. *J. Biomech. Engng* **121**, 170–177.
- Ismagilov, R. F., Stroock, A. D., Kenis, P. J., Whitesides, G. M. & Stone, H. A. 2000 Experimental and theoretical scaling laws for transverse diffusive broadening in two-phase laminar flows in microchannels. *Appl. Phys. Lett.* **76**, 2376–2378.
- Kamholz, A. E. & Yager, P. 2001 Theoretical analysis of molecular diffusion in pressure-driven laminar flow in microfluidic channels. *Biophys. J.* **80**, 155–160.
- Kataoka, D. E. & Troian, S. M. 1997 A theoretical study of instabilities at the advancing front of thermally driven coating films. *J. Colloid Interface Sci.* **192**, 350–362.
- Kataoka, D. E. & Troian, S. M. 1999 Patterning liquid flow on the microscopic scale. *Nature* **402**, 794–797.
- Knight, J. B., Vishwanath, A., Brody, J. P. & Austin, R. H. 1998 Hydrodynamic focusing on a silicon chip: mixing nanoliters in microseconds. *Phys. Rev. Lett.* **80**, 3863–3866.
- Liu, R. H., Stremmer, M. A., Sharp, K. V., Olsen, M. G., Santiago, J. G., Adrian, R. J., Aref, H. & Beebe, D. J. 2000 Passive mixing in a three-dimensional serpentine microchannel. *J. MEMS* **9**, 190–197.
- Miyake, R., Lammerink, T. S. J., Elwenspoek, M. & Fluitman, J. H. J. 1993 Micro mixer with fast diffusion. In *Proc. IEEE Micro Electro Mechanical Systems, Fort Lauderdale, FL*, pp. 248–253. New York: IEEE Press.
- Pollack, M. G., Fair, R. B. & Shenderov, A. D. 2000 Electrowetting-based actuation of liquid droplets for microfluidic applications. *Appl. Phys. Lett.* **77**, 1725–1726.
- Rhines, P. B. & Young, W. R. 1983 How rapidly is a passive scalar mixed within closed streamlines? *J. Fluid Mech.* **133**, 133–145.
- Schwesinger, N., Frank, T. & Wurmus, H. 1996 A modular microfluid system with an integrated micromixer. *J. Micromech. Microengng* **6**, 99–102.
- Stroock, A. D., Dertinger, S. K. W., Ajdari, A., Mezic, I., Stone, H. A. & Whitesides, G. M. 2002 Chaotic mixer for microchannels. *Science* **295**, 647–651.
- Taylor, G. I. 1953 Dispersion of soluble matter in solvent flowing slowly through a tube. *Proc. R. Soc. Lond. A* **219**, 186–203.